



# Characterization of zirconium oxides part II: New insights on the growth of zirconia revealed through complementary high-resolution mapping techniques

Corey M. Efaw<sup>a,b</sup>, Jordan L. Vandegriff<sup>a,b</sup>, Michael Reynolds<sup>a</sup>, Brian J. Jaques<sup>a,b</sup>, Hongqiang Hu<sup>c</sup>, Hui Xiong<sup>a,b</sup>, Michael F. Hurley<sup>a,b,\*</sup>

<sup>a</sup> Micron School of Materials Science and Engineering, Boise State University, 1910 W University Dr, Boise, ID, 83725, USA

<sup>b</sup> Center for Advanced Energy Studies, 995 University Blvd, Idaho Falls, ID, 83401, USA

<sup>c</sup> Idaho National Laboratory, 2525 Fremont Ave, Idaho Falls, ID 83402, USA

## ARTICLE INFO

### Keywords:

Zirconium alloys  
Cladding  
Oxidation  
Raman mapping  
SKPFM  
SEM/EDS

## ABSTRACT

Raman mapping, scanning Kelvin probe force microscopy (SKPFM), and scanning electron microscopy with energy dispersive X-ray spectroscopy (SEM/EDS) were combined to investigate oxidized zirconium alloys. Raman provided spatially resolved phase composition and relative stress state. When coupled with SKPFM, phase composition was correlated to Volta potentials differences. The potential of tetragonal zirconia was lower than the metal zirconium, making the tetragonal phase favorable for reaction with diffusing species, thus hindering further oxidation of the relatively cathodic metal. This provides new insight to the theory of the tetragonal phase being an oxidation barrier.

## 1. Introduction

The adverse environment created from irradiation and variable conditions within a nuclear reactor core induces complex degradation processes of cladding. Zirconium alloys are a viable material choice for fuel cladding, due to its low neutron absorption cross-section and strong corrosion resistance while in a nuclear reactor environment. Dynamic material effects and the extreme environment make it difficult to predict or monitor cladding condition in-core and present significant obstacles for achieving a comprehensive and unified understanding of cladding degradation mechanisms [1–4].

Currently, chemical evolution over the lifetime of cladding can only be inferred using post-irradiation examination (PIE) [5], or mimicking the coolant-side conditions with in-situ characterization [6–10]. Progress is being made to establish new sensing techniques; for instance, electrochemical impedance spectroscopy (EIS) is becoming established as a cladding degradation sensing technique [5–7]. However, in order to develop accurate EIS models and advance current sensor technology, high-resolution characterization techniques must be used to translate degradation processes along the cladding pathway to equivalent circuit models. This work utilizes scanning Kelvin probe force microscopy (SKPFM), Raman spectroscopy, and scanning electron microscopy (SEM) with energy-dispersive X-ray spectroscopy (EDS) to provide

high-resolution co-localized characterization of zirconium oxide and metal/oxide interface.

Raman spectroscopy provides qualitative to semi-quantitative information on ceramic material composition. This technique has been extensively used for both *in-situ* and post-exposure sectioned analysis of zirconium alloys [8–13]. Raman provided evidence of a bilayer oxide structure grown on zirconium after extended thermal oxidation [14,15]. The inner layer is a metastable tetragonal phase that has been considered on both ends of the spectrum with regards to being either a protective barrier or a non-participant in the corrosion mechanism of the cladding [3]. The metastable tetragonal phase is believed to be stabilized by a combined effect of interfacial compressive stress, oxygen sub-stoichiometry, and grain size [8,9]. Via a martensitic phase transformation, tetragonal zirconia transitions to a columnar grained and more porous monoclinic zirconia outer layer. A region of mixed, transient tetragonal-monoclinic zirconia exists between these layers. Raman spectra also provide insight into the stress distribution within the oxide, where high compressive stress is seen in the small, equiaxed tetragonal grains near the metal/oxide interface. With support by oxide porosity, this high compressive stress is believed to reach a critical value that is followed by a rapid transition to a less stressed state. The stress relief, termed the breakaway phenomenon, is allowed by vertical fracturing in the oxide, providing a pathway for increased oxidation rate [3,13].

\* Corresponding author at: Micron School of Materials Science and Engineering, Boise State University, 1910 W University Dr, Boise, ID, 83725, USA.

E-mail address: [mikehurley@boisestate.edu](mailto:mikehurley@boisestate.edu) (M.F. Hurley).

<https://doi.org/10.1016/j.corsci.2020.108491>

Received 6 September 2019; Received in revised form 22 January 2020; Accepted 23 January 2020

Available online 23 January 2020

0010-938X/ © 2020 Elsevier Ltd. All rights reserved.

SKPFM is a non-destructive atomic force microscopy (AFM) variant that resolves nanoscale features on the material surface. The traditional Kelvin probe utilizes the capacitive nature between conductors in electrical contact to determine the contact potential difference (CPD), or Volta potential difference (VPD). When applied to a nanoscale and mobile probe, SKPFM spatially resolves local relative Volta potentials that correspond to microstructural heterogeneities on the material's surface. The VPD between two metals in electrical contact directly relates to the difference in their electron work functions [16]. While in an inert environment with minimum surface adsorbates, the Kelvin probe can theoretically acquire the work function difference between probe and sample surface. It is a useful surface characterization technique for specifying phase nobility (i.e., microgalvanic coupling) [17–22], hydrogen precipitation detection [23–27], characterization of semiconductors [28,29], and co-localization with elemental makeup from SEM/EDS [30]. However, SKPFM has yet to be utilized for characterizing nuclear cladding zirconium alloys. The thermally grown zirconia is an n-type semiconductor, where oxide growth at the cladding's metal/oxide interface is limited by oxygen anion diffusion [3]. With the existence of an electric field driving spontaneous high-temperature corrosion, the flux of oxygen anions to the metal is balanced by a flux of electrons to the oxide/coolant boundary via hopping mechanism, thus netting zero current [3,4]. The ionic conductivity of zirconia is ultimately driven by crystal lattice defects, such as Frenkel defects, Schottky disordering, dislocations, and grain boundaries [4,31]. A region of oxide bordering the metal substrate, stabilizes as tetragonal zirconia due to high compressive stress and oxygen sub-stoichiometry [8–10,32], making it a viable electron acceptor (i.e., p-type semiconductor). This thin tetragonal phase is theorized to be a barrier layer to increased oxide growth [3]. Additionally, distribution of other species in zirconia produce spatial heterogeneities in electronic properties, and thus provide a driving force for microgalvanic reactions to occur [33]. Given these notable variabilities in the oxide structure, the nanoscale resolution capabilities of SKPFM can provide spatial mapping of ionic/electronic pathways that regulate the corrosion mechanism. SKPFM can provide new insight into the electronic properties of the zirconia layering, oxygen stoichiometry, and metal/oxide interface. Additionally, SKPFM could be utilized to detect heterogeneities such as secondary-phase precipitates, hydrides, and nitrides.

The electronic structure of both oxide and metal has great effect on the catalytic activity at the metal/oxide interface. Also, the inclusion of alloying elements plays a role in catalytic activity and selectivity of metals [34]. An ensemble of carefully selected complementary characterization techniques enables new correlations between electronic properties, microstructural heterogeneities, and elemental composition. These correlations provide an insight of zirconia growth mechanisms yet to be observed with individual techniques. With an improved knowledge of cladding degradation, accurate EIS equivalent circuit models can be used for in-core monitoring of cladding degradation.

## 2. Experimental methods

Zirconium (Goodfellow) and Zr-2.65Nb (ATI Metals) were chosen for the current work (Table 1). Plate samples were isothermally oxidized, with thermogravimetric analysis (TGA) used to monitor mass gain rate, as described elsewhere [35]. Samples were exposed to 80 % N<sub>2</sub>, 20 % O<sub>2</sub> environment at 700 °C. After oxidation, samples were sectioned and mounted in epoxy. They were then ground with SiC up to

**Table 1**  
Zirconium and Zr-2.65Nb compositions.

	Fe	Sn	Cr	Nb	C	Hf	O	N	H	Zr
Zr (ppm)	200	–	200	–	250	2500	1000	100	10	bal.
Zr-2.65Nb (wt. %)	0.061	–	–	2.62	–	–	0.106	–	–	bal.

1200 grit, followed by polishing with 1 and 0.05 μm alumina slurries. Following polishing, samples were cleaned with heated Alconox solution on a soft pad, rinsed with ultrapure water, and air dried. Samples were then immediately transferred to the glovebox AFM for SKPFM analysis.

SKPFM was done with a Dimension Icon AFM (Bruker) in an argon filled glovebox (MBraun, < 0.1 ppm O<sub>2</sub> and H<sub>2</sub>O). PFQNE-AL probes were used to acquire results, operating under a dual-pass method called FM PF-KPFM [36]. In addition to topography, quantitative nano-mechanical (QNM) properties were simultaneously acquired from probe/material interactions. Volta potential differences were acquired when the probe was lifted to a user-defined lift height of 100 nm above the surface, creating a nanoscale scenario synonymous to the traditional Kelvin probe. Prior to SKPFM acquisition of the cladding samples, probes were calibrated by imaging a Bruker PFKPFM-SMPL, consisting of an n-doped silicon substrate with patterned islands of aluminum surrounded by a gold interconnect. This sample was utilized to ensure relative consistency of probes by providing a step-wise VPD map from aluminum to silicon to gold [36]. Image processing and analysis were conducted using NanoScope Analysis V1.8 (Bruker). Topography maps underwent a flattening process to remove sample tilt.

Raman spectroscopy was accomplished using a Horiba LabRAM HR Evolution (Horiba Scientific) with a monochromatic 532 nm doubled Nd:YAG laser with 50 mW power and ~0.3 μm spectral resolution. Samples were mounted on a motorized stage with ± 1 μm X–Y repeatability and accuracy. Spatial resolution depended upon objective lens magnification, ranging from 721 nm to 1.18 μm, and thus Raman maps were acquired with 1 μm spacing between collected spectra. Spectral range of 150–700 cm<sup>-1</sup> was used to examine peaks of interest. Spectra were processed and analyzed with LabSpec V6.3.x (Horiba). Spectral arrays underwent a baseline correction to remove background noise. Convolution of Gaussian and Lorentzian peak fitting was collected for spectral arrays. Peak position and amplitude were collected for different peaks in each spectrum and formed into X–Y maps. Distinction of zirconia phase, particularly monoclinic and tetragonal, has been well established [11]. Tetragonal phase, which is thermodynamically stable above 1205 °C [37], is stabilized at lower temperatures in the grown oxide. The stability of tetragonal phase near the metal/oxide interface is driven by high compressive stress and oxygen sub-stoichiometry [8]. Phase content (i.e., volume fraction) of tetragonal and monoclinic zirconia is estimated to calculate the named percent tetragonality. The first tetragonal peak (T<sub>1</sub>) versus neighboring monoclinic peaks (M<sub>3</sub> and M<sub>4</sub>) was decidedly used to calculate percent tetragonality (Eq. 1). Also analyzed from Raman spectra was relative residual stress, where shifts in monoclinic peak positions directly correlates to relative stress [13]. The M<sub>2</sub> peak was chosen to observe relative residual stress, where a decrease in this peak's position correlates with increasingly relative compressive stress. A calibration is commonly done in order to quantify stress – however, a calibration was not conducted for this work. Rather, the relative stress state was observed to show trends as a function of percent tetragonality and distance from the metal/oxide interface.

$$\%T_{ZrO_2} = \frac{I(T_1)}{I(M_3) + I(T_1) + I(M_4)} \quad (1)$$

SEM/EDS with a Hitachi S-3400N-II (Oxford Instruments Energy +) at 10–15 keV and 10 mm working distance to provide elemental distribution of each sample. Due to the inherent sample damage that occurs during Raman (laser beam damage [38]) and SEM/EDS (carbon pyrolysis and electron beam irradiation [21,22,30]), these techniques were done in corresponding order after SKPFM. In addition, samples were carbon-coated prior to SEM/EDS to provide a conductive layer over the epoxy mount and inhibit charge build-up.

## 3. Results and discussion

TGA provided observable mass gain rate for the zirconium samples

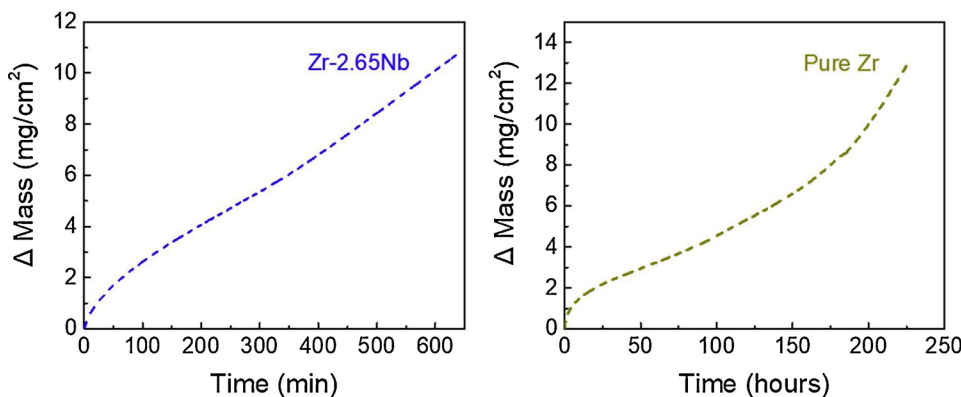


Fig. 1. Normalized mass gain during isothermal oxidation for Zr-2.65Nb (left) and Zr (right).

(Fig. 1). Samples were held to points either before or after breakaway was observed. Breakaway was identified by a transition of mass gain rate from parabolic to linear kinetics. Faster kinetics and breakaway are induced much earlier in air than seen in oxygen or steam environments, due to the inclusion of nitrogen in the mechanism. Nitride formation and subsequent oxidation of those nitrides leads to increased porosity of the oxide [35]. The post-breakaway pure Zr sample was oxidized for  $\sim 226$  h, while the post-breakaway Zr-2.65Nb was oxidized for  $\sim 10.5$  h. An additional pure Zr sample was oxidized for 20 h, being removed prior to breakaway occurring. The vast superiority of Zr over Zr-2.65Nb in resisting corrosion and breakaway is opposite of water-side corrosion performance, where inclusion of niobium improves corrosion and breakaway resistance, as well as mechanical properties when compared to pure zirconium [3]. In the case of this study, exposure to high temperature mixed nitrogen/oxygen environment presents different possible scenarios mimicking an air-cooled core (such as with Transient Reactor Test Facility (TREAT) at Idaho National Lab) or air ingress and rapid increase in temperature during a nuclear reactor loss-of-coolant accident (LOCA). Corrosion mechanisms in this particular environment are described elsewhere [35].

Post-oxidation analysis was done on cross sectioned samples. Being the least destructive technique, SKPFM in an argon filled glovebox was done first. Co-localization of SKPFM with the other techniques was accomplished by establishing fiducial marks, such as distinct crack morphology in the oxide or variation in oxide/metal profile.

For SKPFM, relative Volta potentials (i.e., Volta potential difference, VPD), as well as QNM properties were mapped and used to identify the exact metal/oxide boundary. Fig. 2 presents height, VPD, adhesion, and deformation acquired for the oxidized Zr sample. The metal/oxide interface is noted with red lines. A clear boundary is seen between the metal and oxide, where the average metal Volta potential is  $\sim 160$  mV higher than the average oxide Volta potential (Fig. 2b). Differences in surface morphology (Fig. 2a), as well as changes in adhesion (Fig. 2c) and deformation (Fig. 2d) support that the transition point between metal and oxide correspond with the boundary in the Volta potential channel. In addition, a large particle is seen at the metal/oxide interface, displaying higher Volta potential than the surrounding oxide and metal. Based upon the size and location of the particle, as well as the exposing environment, it is likely either a secondary-phase precipitate (SPP) or a nitride. During breakaway in a mixed nitrogen/oxygen environment, nitride particles form at the metal/oxide interface [35]. The difference in lattice density between Zr,  $\text{ZrO}_2$ , and  $\text{ZrN}$  causes lattice mismatch, driving cracking and formation of porous oxide following the oxidation of the nitride particle, leading to pathways for increased cladding degradation [39–41]. On the other hand, elements such as chromium and iron can form SPPs that tend to oxidize at a slower rate than the surrounding zirconium matrix. These slow oxidizing SPPs may support microgalvanic corrosion of the surrounding zirconium, as well as provide pathways via lattice mismatch to cause cracking of the oxide

[3]. At higher temperatures, the mobility of iron and chromium should increase, allowing possible formation of SPPs, even when low in concentration. The higher measured Volta potential of the particle seen in Fig. 2 supports the theory that it acts as a local cathode relative to the surrounding oxide.

Raman mapping of the same area provided insight into the separation of oxide phases. Fig. 3 shows maps of both percent tetragonality (i.e., phase content) and monoclinic peak position (i.e., relative stress state). At the metal/oxide interface (metal is gray in color), tetragonal-rich phase is evident, as are shifts to lower monoclinic peak position that corresponds to increasing compressive stress. As the distance from the interface increases, relative stress decreases, as does the concentration of tetragonal phase. There are notable regions in the bulk oxide with higher percent tetragonality, which may correspond to the “relaxed-tetragonal” phase. It has been shown that this other tetragonal phase stabilizes in the bulk of the oxide via sub-stoichiometry, absent of compressive stress supporting its formation. However, in the case of a few of the tetragonal-rich regions in the bulk of the oxide, a notable correlation between high tetragonality and compressive stress is seen. Looking at the SEM image showing the collected Raman map (Fig. 3c), these regions appear to be near a large horizontal crack, along with highly porous oxide.

A particular region in the bottom left of the Raman map in Figure 3 was further investigated to determine the reason for high compressive stress in the bulk of the oxide. Considering the spectra along the line in Fig. 4, a few observations can be made. The spectra that have lower monoclinic peak position and tetragonal-rich peaks are noted in Fig. 4c. A majority of spectra with high compressive stress (i.e., low monoclinic peak position) correlate with the presence of tetragonal-rich phase. Two spectra contradict this correlation at  $X = 30 \mu\text{m}$  and  $38 \mu\text{m}$ . For the former, the tetragonal peak is near  $265 \text{ cm}^{-1}$ , which is different than tetragonal peak positions seen in the other spectra ( $275 - 285 \text{ cm}^{-1}$ ). Additionally, there is a lessened presence of compressive stress, as the monoclinic peak is positioned at a higher wavenumber. These factors correspond with the relaxed-tetragonal phase, where relaxed-tetragonal peak position is lower than peak position of tetragonal phase stabilized by compressive stress [8]. For the  $X = 38 \mu\text{m}$  spectra, it appears that high compressive stress is present, but no tetragonal peak is observed. This appears to be the transition point from the tetragonal-rich region to monoclinic-rich, even though there is still high compressive stress. These observations support the theory that oxygen sub-stoichiometry must be present with notable compressive stress to stabilize tetragonal phase [8]. For all other spectra with noted tetragonal phase ( $X = 32 - 37 \mu\text{m}$ ), the location of the tetragonal peaks are at  $275 - 285 \text{ cm}^{-1}$ , corresponding with what is typically seen for stress-stabilized tetragonal phase. Additionally, the  $M_2$  peak position for these spectra supports presence of a relative compressive stress with lower peak positions. Therefore, the stabilization of this tetragonal zirconia is driven by both oxygen sub-stoichiometry and compressive stress, much

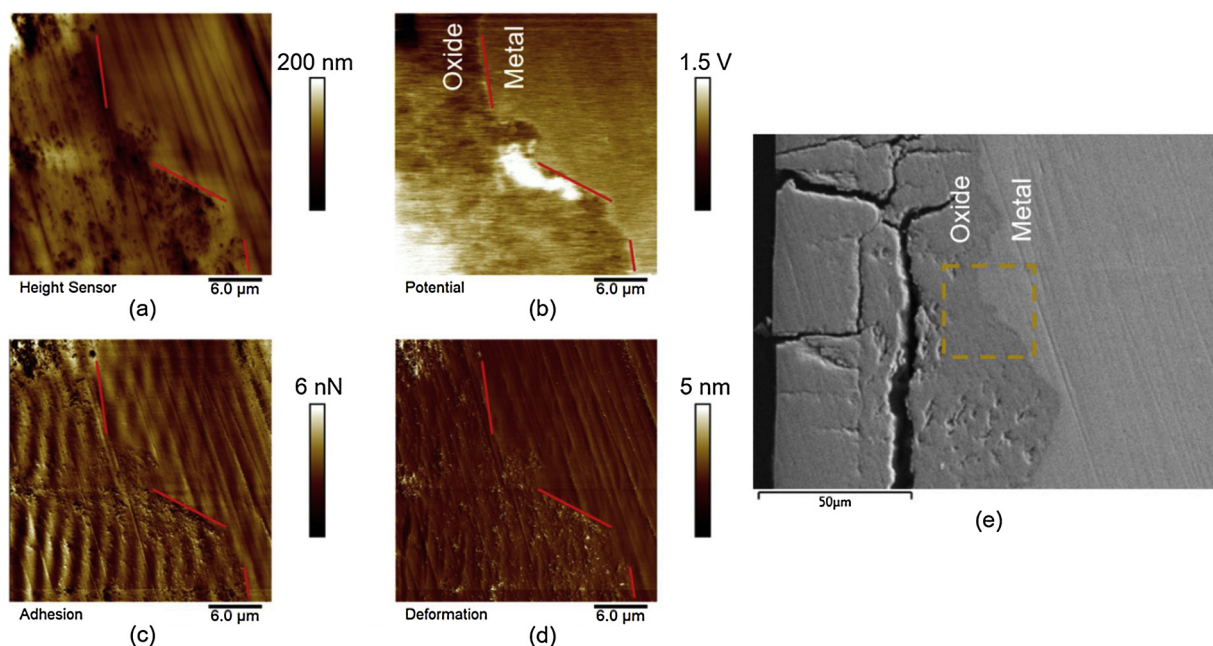


**Fig. 2.** AFM results for sectioned sample of oxidized Zr. (a) Height, (b) relative Volta potential, (c) adhesion, and (d) deformation images with red lines separating metal and oxide. (e) SEM image with area where SKPFM was performed. (For interpretation of the references to colour in this figure legend, the reader is referred to the web version of this article.)

like the tetragonal phase present near the metal/oxide interface. The presence of the large crack close to this zirconia may support the change in stress state and thus stabilization of tetragonal phase.

Correlations between the SKPFM and Raman maps were also made. Within the Raman tetragonality map (Fig. 3a), at the metal/oxide interface there is an area of lower percent tetragonality with similar shape and size to the cathodic particle seen with SKPFM (Fig. 2b). A closer look at this particle is seen in Fig. 5. The data acquired via SKPFM (Fig. 5a), Raman mapping (Fig. 5b-c), and SEM/EDS, (Fig. 5d) follow a

line that crosses the cathodic particle. Co-localization of X-Y position for each technique was done by aligning the distance from the metal/oxide interface to other notable features. The Volta potential for the particle is  $\sim 600$  mV greater than the neighboring metal, displaying relative cathodic nature (Fig. 5a). This particle's Volta potential maximum is at the same point as the largest decrease in  $M_2$  peak position, and thus largest relative compressive stress (Fig. 5c). Additionally, this occurs when percent tetragonality is increasing, but is still below its maximum value (Fig. 5b). The end of the oxide, where percent

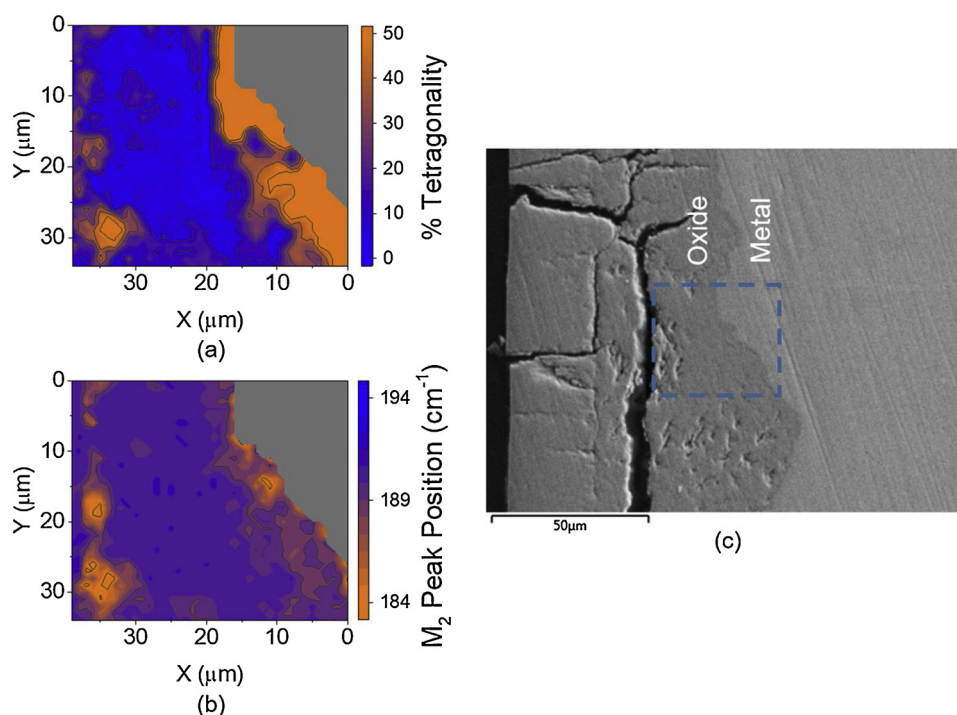


**Fig. 3.** Raman mapping results for sectioned sample of oxidized Zr. (a) Percent tetragonality and (b) monoclinic ( $M_2$ ) peak position maps. (c) SEM image with area where Raman mapping was performed.



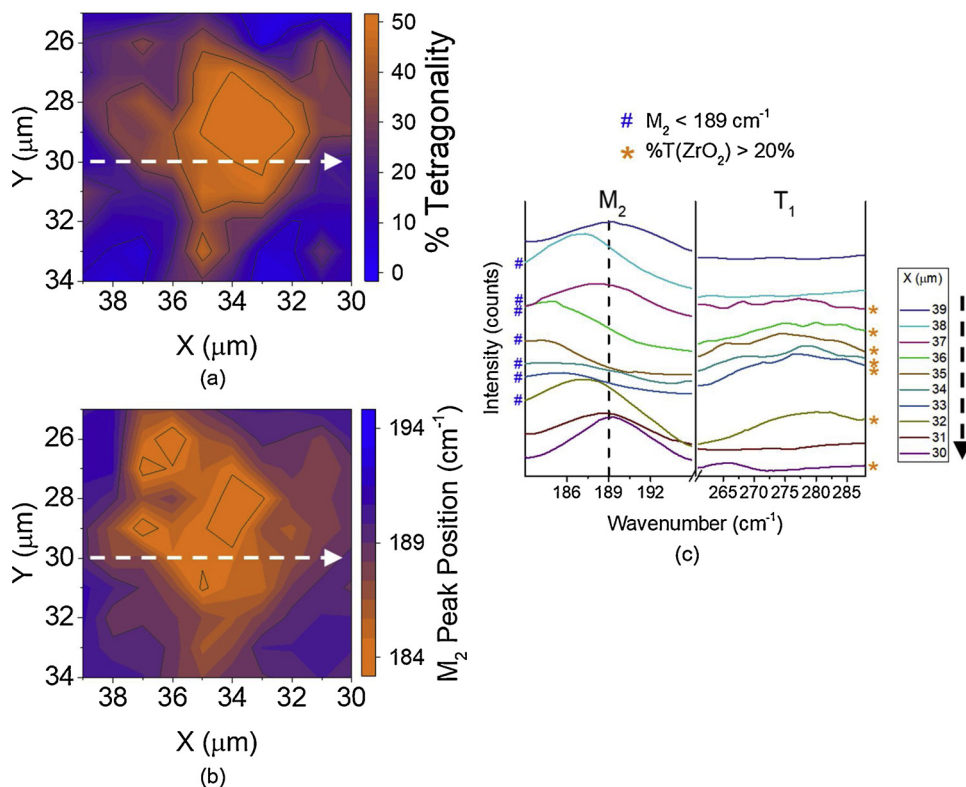


Fig. 4. (a) Percent tetragonality and (b) monoclinic zirconia ( $M_2$ ) peak position maps of region within Raman mapped area in Fig. 3. (c) Raman spectra across dotted line in (a–b), focusing on  $M_2$  and tetragonal zirconia ( $T_1$ ) peak positions. Spectra labeled with a blue '#' present  $M_2$  peaks corresponding to compressive stress (i.e., notably lower peak position). Spectra labeled with an orange '\*' present tetragonal peaks warranting tetragonal-rich spectra via Eq. 1. (For interpretation of the references to colour in this figure legend, the reader is referred to the web version of this article.)

tetragonality and  $M_2$  peak position lines abruptly end, is where the particle ends.

Further evidence of either nitride or iron-enrichment for this particle can be seen in Fig. 6, showing individual Raman spectra across a portion of the noted line scan in Fig. 5. Spectra nearest the metal/oxide interface (i.e., near  $X = 8 \mu\text{m}$ ) reveal a high relative tetragonal peak around  $280 \text{ cm}^{-1}$ . As the distance from the metal/oxide interface increases, evidence of a broad peak around the  $200 - 250 \text{ cm}^{-1}$  range is seen. The broad peak in this region can help explain why the percent tetragonality map revealed a particle of lower tetragonality with similar shape to the high Volta potential particle. It is likely due to the  $M_3$  monoclinic peak being used to support calculation of percent tetragonality (Eq. 1). Since the broad peak arises in this spectral range, it is recognized as the ' $M_3$  peak', when in actuality a different compositional feature is revealed. Further away from the metal/oxide interface, this broad peak is slowly lost (Fig. 6), and the sharp  $M_3$  peak is revealed (i.e.,  $X = 17 - 19 \mu\text{m}$ ). The broad peak shows similar spectral features as those seen in ZrN [11], as well as hematite ( $\text{Fe}_2\text{O}_3$ ) [42]. For ZrN, a sharp peak is seen in the  $230 - 235 \text{ cm}^{-1}$  range, with a broad shoulder to the left to  $\sim 170 \text{ cm}^{-1}$ . For hematite, the  $A_{1g}$  mode at  $225 \text{ cm}^{-1}$  and its shouldering  $E_g$  mode at  $247 \text{ cm}^{-1}$  are similar to the spectral features of the broad peak. Due to the shape of this broad peaks seen in Fig. 6, it is reasonable to conclude that the particle is an iron-rich SPP. The shouldering that is visible to the right of the broad peak likely correlates to the  $E_g$  mode of hematite, while ZrN has a shouldering to the left of its peak. In addition, the Fe-rich SPP is likely highly metallic, thus producing Raman spectra with high amounts of noise. The oxidation of cathodic SPPs are slow relative to Zr, thus leaving a heavily metallic particle in an oxidized matrix [3].

For compositional correlation, a line scan of EDS measurements is included (Fig. 5d). There is no discernable evidence of concentrated iron or nitrogen counts near the metal/oxide interface. A possible reason for this lack of secondary element response may be due to the damage inflicted upon the sample from the 50 mW Raman laser. When laser power is increased, there is a tradeoff between maximizing signal and increasing surface damage. Damage to the sample surface from the

Raman laser makes it difficult to resolve particles even a few microns in size with SEM/EDS. Further evidence of this effect can be seen in Fig. 7, where a Zr pre-breakaway sample correlates high Volta potential particles and iron-rich SPPs. Raman mapping was excluded in the analysis of this sample, thus excluding the possible effect of Raman laser damage prior to SEM/EDS. This provides evidence of SPP formation in the Zr sample, regardless of the low concentration of iron in pure Zr (Table 1). Therefore, the absence of iron in the EDS line scan in Fig. 5d does not restrict iron from being the contributing element to the cathodic behavior of the particle.

To observe the metal/oxide interface and similarities between features, Fig. 8 shows co-localized maps with corresponding line scan data plots for each technique. In this case, a direct transition between metal and oxide is seen at  $X \approx 8 \mu\text{m}$ . This occurs where the Raman spectra ends, as well as where a sharp transition in Volta potential is seen. The tetragonal-rich region can be distinguished in the  $X = 8 - 20 \mu\text{m}$  range (Fig. 8b). A drop in Volta potential is visible in this range, providing evidence that the tetragonal-rich region nearest the metal/oxide interface is relatively anodic versus the metal. In fact, the only region within the captured SKPFM image that shows a higher relative Volta potential is in the bottom left area of the image (Fig. 8a). This region likely correlates to monoclinic-rich zirconia, while the rest of the zirconia mapped in the SKPFM image is tetragonal-rich, and thus lower in relative Volta potential.

Co-localized SKPFM, Raman mapping, and SEM/EDS was also performed on the sectioned Zr-2.65Nb sample (Fig. 9). Contrary to Zr, the average Volta potential of the oxide is  $\sim 685 \text{ mV}$  greater than that of the metal, revealing relative cathodic behavior for the oxide and relative anodic behavior for the metal (Fig. 9a). The Raman map reveals a tetragonal-rich region at the metal/oxide interface, while the bulk of the oxide is monoclinic-rich (Fig. 9b). Similarly, compressive stress is seen in the form of lower  $M_2$  peak position for zirconia nearest the metal/oxide interface, while the bulk of the oxide is relatively close to the expected  $M_2$  peak position of  $189 \text{ cm}^{-1}$  (Fig. 9c). Looking at the line scans across the metal/oxide interface, correlations between phase content and VPD can be made. A rapid decline in Volta potential is seen

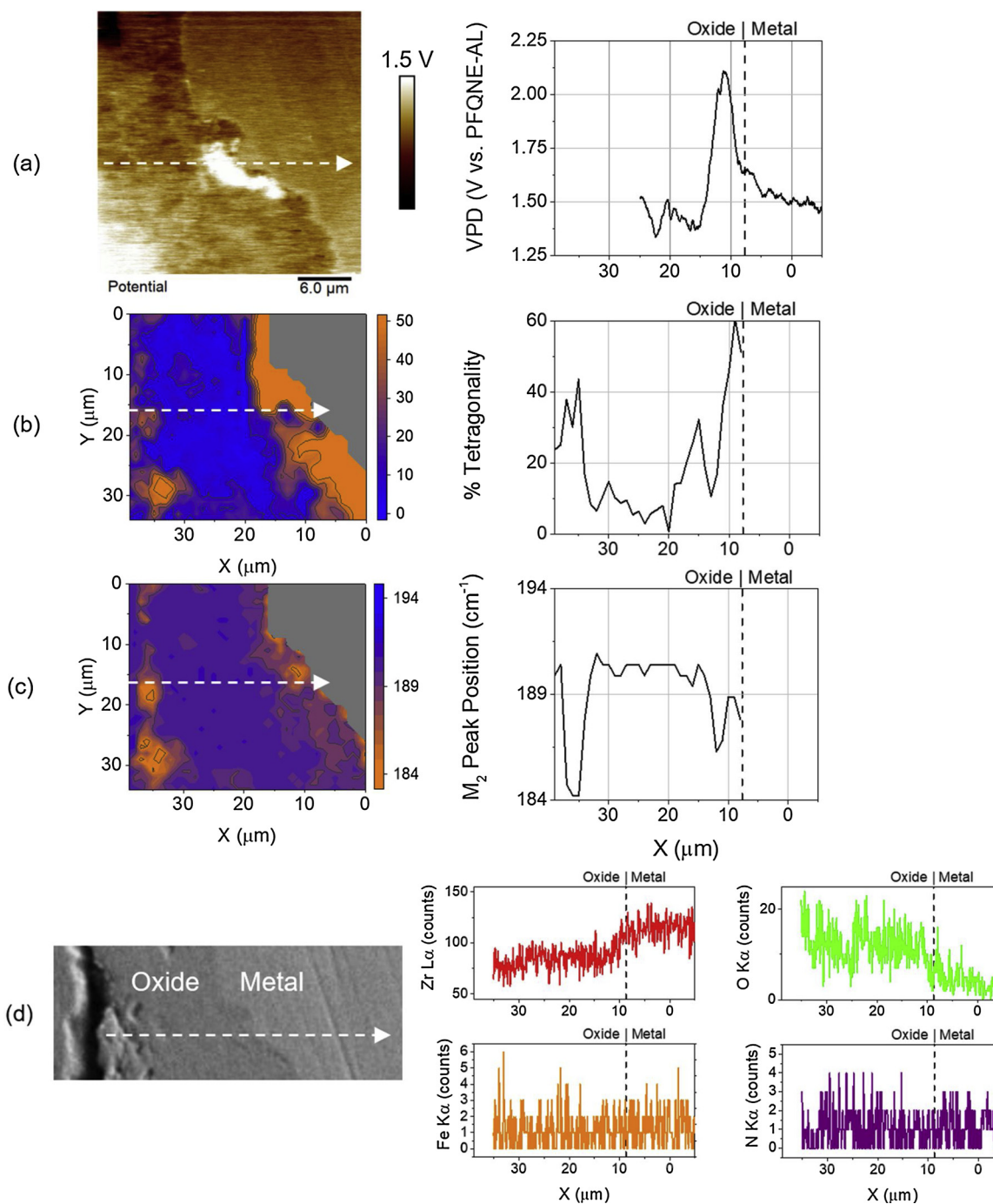


**Fig. 5.** Co-localization between (a) SKPFM Volta potential map with VPD line scan of 1 V range, (b) percent tetragonality and (c)  $M_2$  peak position maps with line scans determined via Raman mapping, and (d) SEM image with EDS elemental line scans for a sectioned sample of oxidized Zr.

at the same position as an increase in percent tetragonality and decrease in  $M_2$  peak position. In the VPD line scan, there is a thin trench that corresponds to the tetragonal-rich zirconia seen in Fig. 9b. After this trench, the VPD slightly increases, coordinating to the Zr-2.65Nb metal. This supports the evidence seen from Zr, where tetragonal-rich zirconia has a lower Volta potential than both the monoclinic-rich zirconia and the metal. A clear metal/oxide boundary is seen in the EDS maps. Due to the substitutional mechanism of Nb in zirconium, no SPPs were seen with EDS. Similarly, no discernible particles were seen in the SKPFM or Raman maps.

The tetragonal phase zirconia at the metal/oxide interface has been recognized as a protective barrier, providing a dense layer that limits the oxidation mechanism by diffusion of oxygen anions. The porous

monoclinic zirconia layer is theorized to provide an easy pathway for coolant media diffusion through the pores and columnar grain boundaries. Once the corrosive media reaches the tetragonal-rich layer, the small, equiaxed tetragonal grains create an oxidation barrier, forcing transport of oxygen anions via vacancy mechanism to reach the metal and form new oxide. A correlation between tetragonal phase stability and oxygen sub-stoichiometry has already been established [10]. Diffusion resistance of the barrier layer correlates with resistance to charge transfer. Moreover, the lower Volta potential for the tetragonal phase implies that it is in fact more active than the surrounding monoclinic zirconia. Here oxidation is supported by the increased oxygen vacancies near the metal/oxide interface. Oxygen concentration gradients have been seen at the metal/oxide interface prior to the martensitic

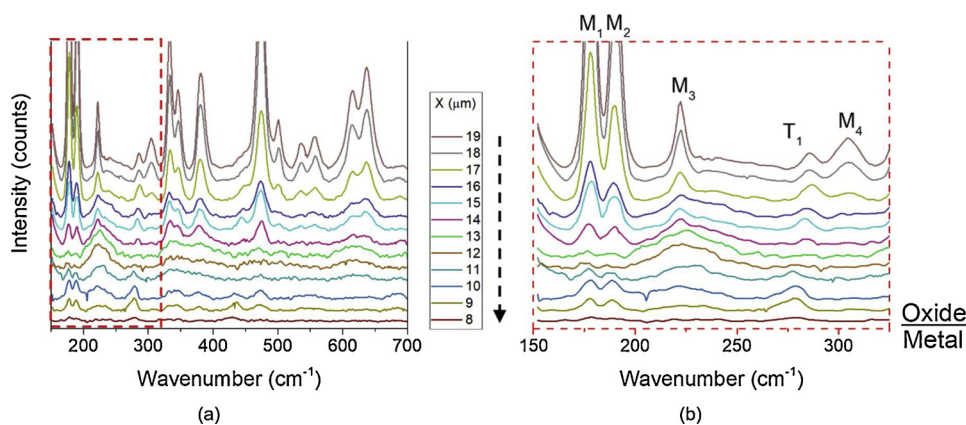


Fig. 6. (a) Raman spectra for partial distance across the line scan in Fig. 5. (b) Inset of spectra with monoclinic (M) and tetragonal (T) zirconia peaks noted.

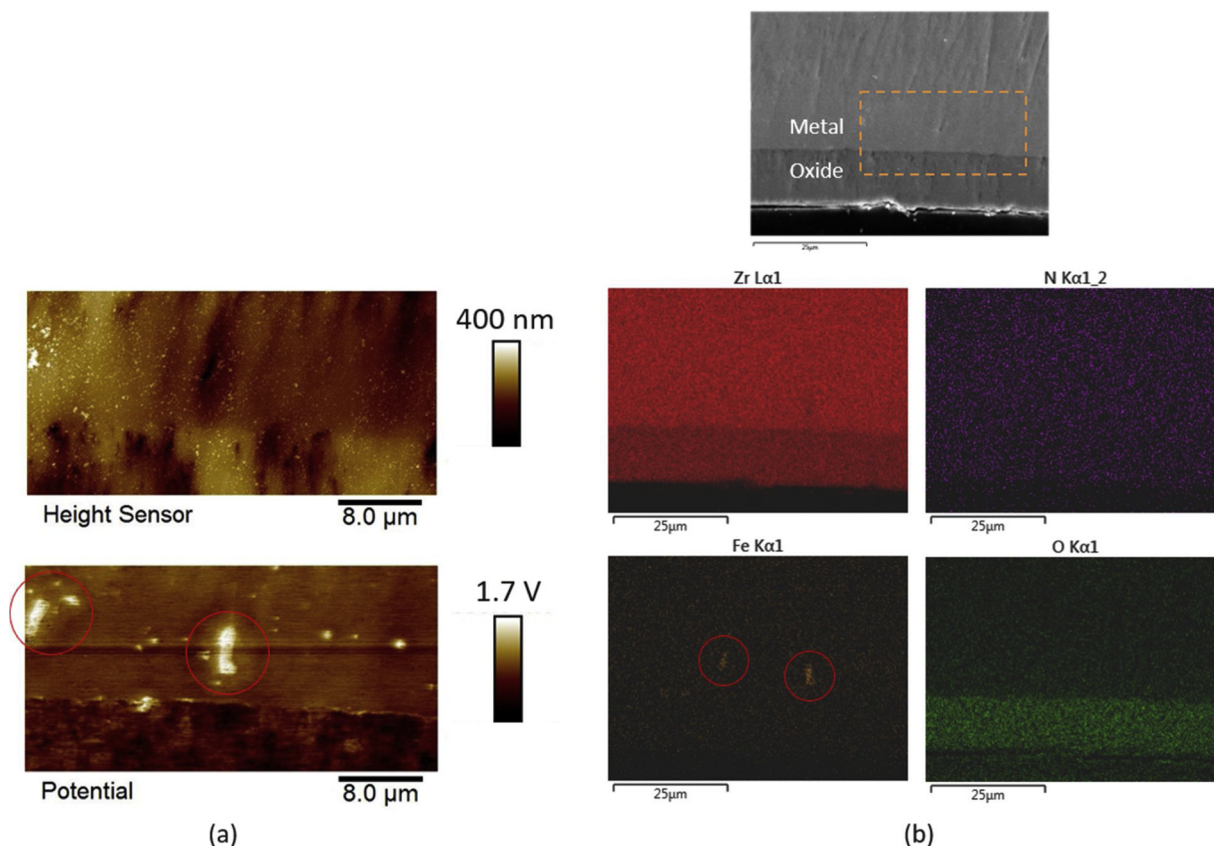


Fig. 7. Co-localization between (a) height and Volta potential via SKPFM and (b) elemental analysis via SEM/EDS for a sectioned sample of oxidized pure Zr (pre-breakaway). Area where SKPFM was performed is included in SEM image. Red circles in Volta potential and EDS maps present correlations between high VPD regions and Fe-rich particles. (For interpretation of the references to colour in this figure legend, the reader is referred to the web version of this article.)

transition to monoclinic phase. This includes a  $Zr(O)_{\text{sat}}$  region of a few hundred nanometers at the metal/oxide interface, followed by a shallow sub-stoichiometric region ( $ZrO_{1-x}$  to  $ZrO_{1+x}$ ) prior to the stable  $ZrO_2$  zirconia [3]. This coordinates with the stability of tetragonal phase, where both compressive stress and oxygen sub-stoichiometry support its formation. The stable monoclinic bulk zirconia has a balanced stoichiometry ( $ZrO_2$ ), whereas the tetragonal zirconia is sub-stoichiometric ( $ZrO_{1-x}$  to  $ZrO_{1+x}$ ). This establishes a p-n junction between the n-type monoclinic zirconia and the p-type sub-stoichiometric tetragonal zirconia. This junction provides an additional barrier for anion transfer to the metal substrate [43]. In addition, the high concentration of holes in this p-type, tetragonal-rich, sub-stoichiometric region causes a reduction in Volta potential relative to the neighboring

metal. This provides further support to the barrier layer theory, where diffusing oxygen anions will need to overcome the p-n junction barrier to progress to the oxide/metal interface.

All metal/oxide parameters discussed are summarized schematically in Fig. 10. The percent tetragonality, stress, Volta potential, and oxygen concentration are shown for different phases of zirconia and zirconium metal. For the metal, the crystal structure is hexagonal closed packed (HCP), under tensile stress, and has minimum oxygen concentration [4]. Crossing the metal/oxide interface, the p-type tetragonal-rich region of zirconia is shown with small, equiaxed grains, high in percent-tetragonality, under high compressive stress, and sub-stoichiometric of oxygen. Further from the metal interface the oxide then undergoes the martensitic phase transformation to an n-type monoclinic zirconia



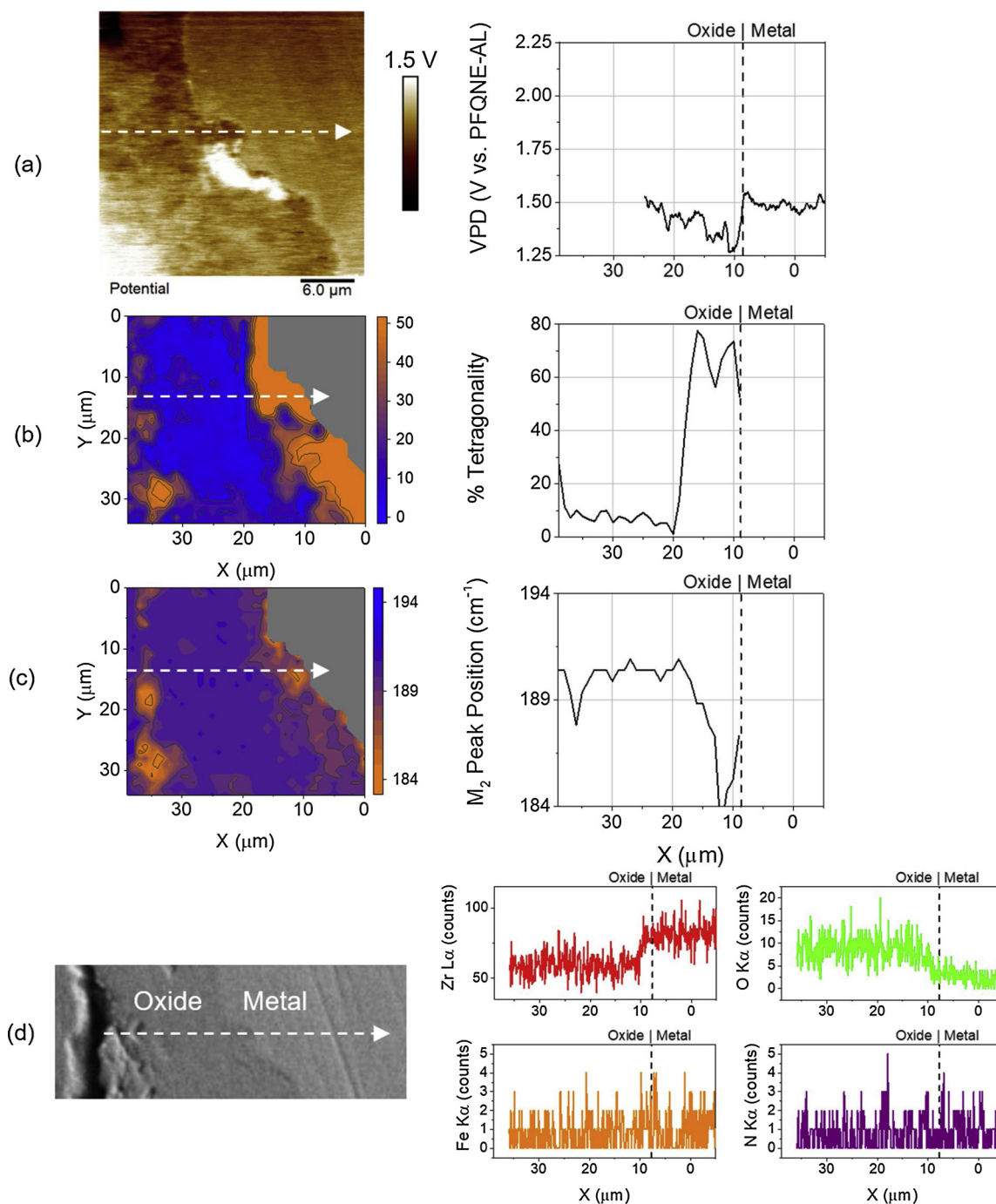


**Fig. 8.** Co-localization between (a) SKPFM Volta potential map with VPD line scan of 1 V range, (b) percent tetragonality and (c) M<sub>2</sub> peak position maps with line scans determined via Raman mapping, and (d) SEM image with EDS elemental line scans for a sectioned sample of oxidized Zr.

phase, where percent tetragonality is at a minimum, compressive stress is lessened, and the lattice is stoichiometric. Additionally, two small grains of relaxed-tetragonal phase are presented in the bulk of the monoclinic oxide. Here, the percent tetragonality slightly increases and oxygen concentration decreases; however, the stress does not deviate from the rest of the bulk oxide. In this region the oxygen sub-stoichiometry supports stabilization of isolated relaxed-tetragonal phase regions, void of compressive stress. A theoretical representation of a decrease in Volta potential of relaxed-tetragonal phase is included. Based upon the measured anodic behavior of the interface-tetragonal phase, the relaxed-tetragonal phase should also hold relative anodic coupling to the neighboring monoclinic phase with a higher Volta potential. Future studies are needed to further understand the electronic

properties and micro-galvanic interactions between oxide phases, secondary particles, and the metal of degraded zirconium cladding.

#### 4. Conclusions

SKPFM was used to characterize sectioned Zr and Zr-2.65Nb metal/oxide interfaces. SKPFM provided electronic properties for microstructural heterogeneities across these interfaces. For Zr, the average VPD of the oxide near the metal/oxide interface was lower than the average VPD of the metal. A cathodic particle was seen at the metal/oxide interface in the post-breakaway Zr sample. For all samples (pre- and post-breakaway Zr, as well as post-breakaway Zr-2.65Nb), the oxide nearest the metal was lower in VPD than the metal; for the post-



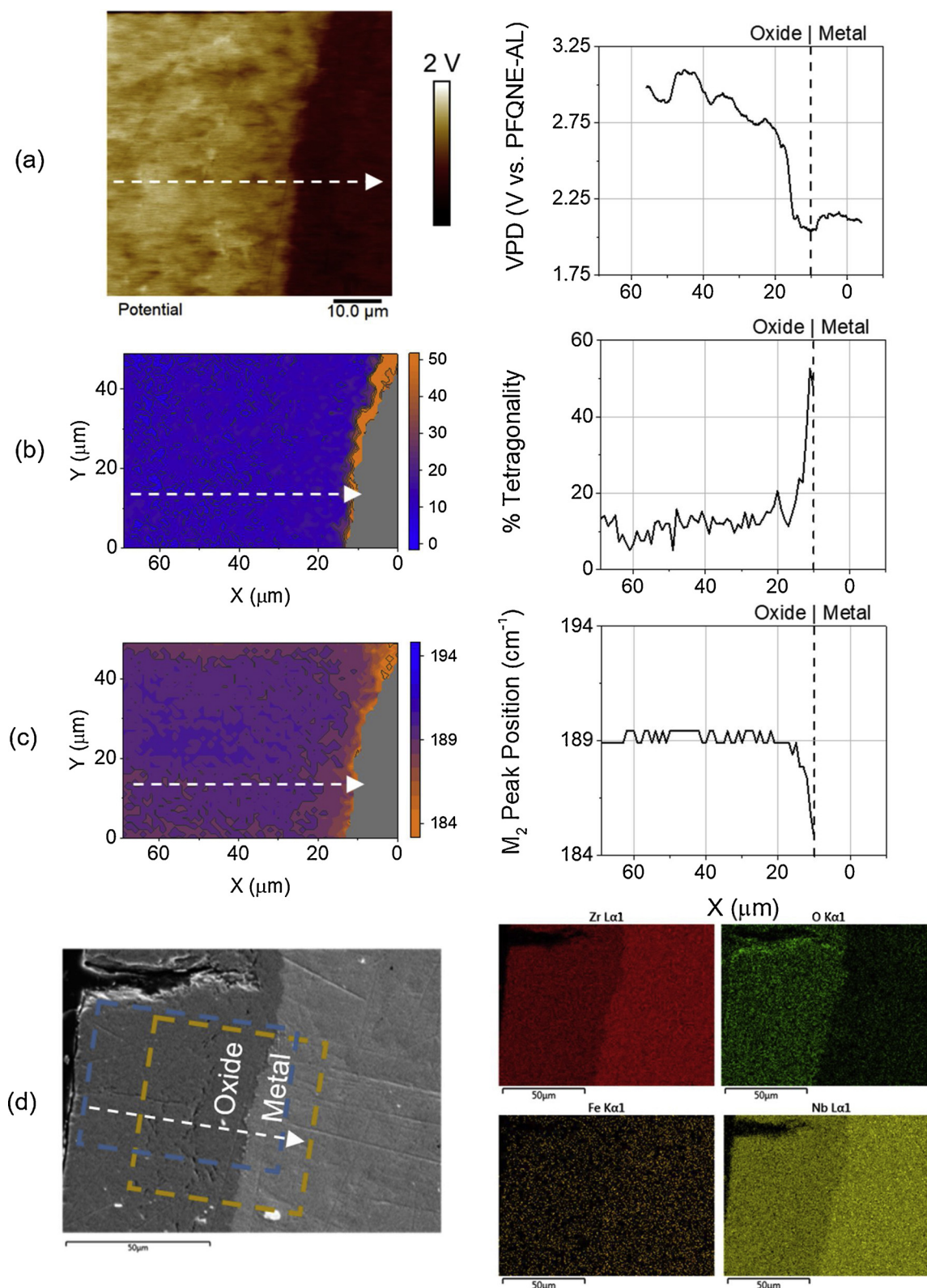


**Fig. 9.** Co-localization between (a) SKPFM Volta potential map with VPD line scan of 1.5 V range, (b) percent tetragonality and (c)  $M_2$  peak position maps with line scans determined via Raman mapping, and (d) SEM image with EDS maps for a sectioned sample of oxidized Zr-2.65Nb.

breakaway Zr-2.65Nb, oxide further from this interface was much higher in VPD.

Raman mapping provided phase and stress distributions for post-breakaway Zr and Zr-2.65Nb. Tetragonal-rich phase was seen near the metal/oxide interface for both samples. Tetragonal phase near the

interface is stabilized from compressive stress and oxygen sub-stoichiometry. The relaxed-tetragonal phase was observed in the bulk of the Zr oxide, while it was not observable in high concentrations in the bulk of the Zr-2.65Nb oxide. The relaxed-tetragonal phase is stabilized by oxygen sub-stoichiometry, voided of compressive stress to support

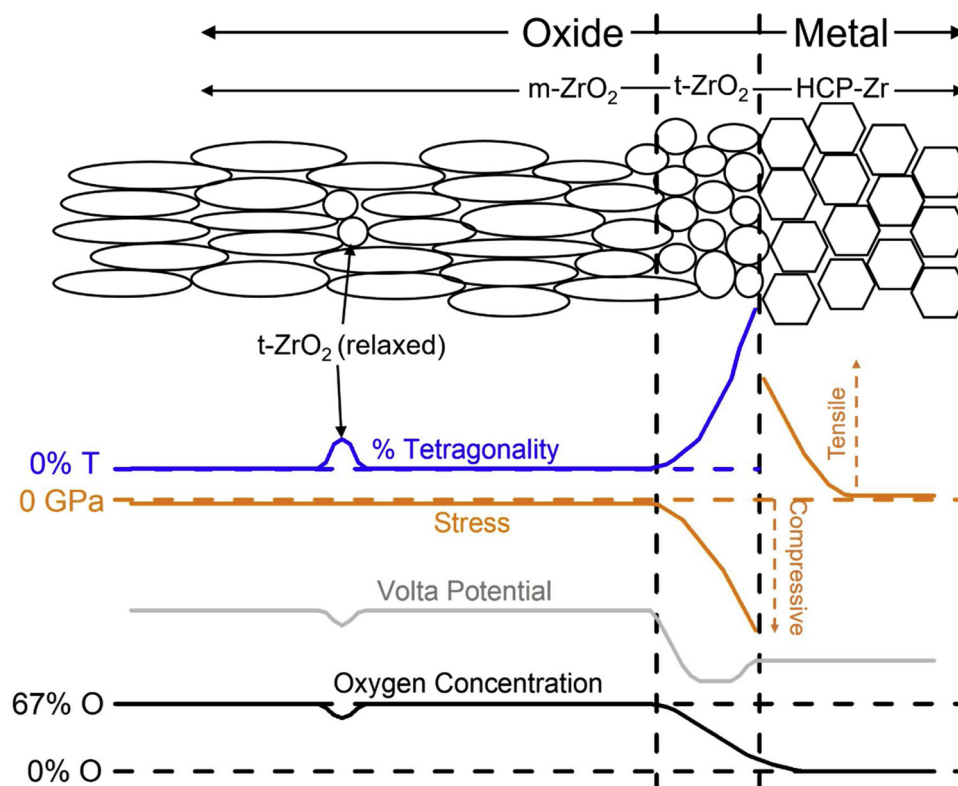


Fig. 10. Schematic summarizing the different parameters for each zirconia and zirconium phase.

stability. Some of the tetragonal phase seen in the bulk of the Zr oxide had a corresponding compressive stress seen by monoclinic zirconia ( $M_2$ ) peak shift to lower wavenumbers. Therefore, tetragonal phase stabilized with support from compressive stress was seen in the bulk of the Zr oxide. This stress-induced tetragonal phase seen in the bulk Zr oxide was likely supported by nearby crack propagation, creating new stress tensors in surrounding oxide.

Co-localization of SKPFM, Raman mapping, and SEM/EDS allowed correlation of different oxide and metal characteristics. For Zr, a broad Raman peak in the  $200 - 250 \text{ cm}^{-1}$  range spatially correlated to the cathodic particle seen with SKPFM. This particle is likely iron-rich, due to the shouldering direction of the characteristic peak and its correlation to the peaks seen in the Raman spectrum of hematite ( $\text{Fe}_2\text{O}_3$ ). Raman laser damage removed the opportunity to observe N and Fe EDS counts to confirm the elemental makeup of the cathodic particle. However, when Raman mapping and related laser damage are omitted, correlations between VPD and elemental makeup of particles can be observed, as confirmed by observation of the pre-breakaway Zr sample. Here, the cathodic secondary particles seen with SKPFM were confirmed as iron-rich with EDS.

For SKPFM/Raman mapping correlations, tetragonal-rich zirconia at the metal/oxide interface correlated to lower VPD than the neighboring zirconium metal and monoclinic zirconia. Raman spectra revealed a thick tetragonal-rich region near the metal/oxide interface, that also had a lower VPD as seen with SKPFM. A small region of higher VPD was seen in the Zr oxide, correlating to the start of the bulk monoclinic-rich zirconia. This was confirmed with co-localized SKPFM and percent tetragonality mapping of the Zr-2.65Nb sample, where a slight drop in VPD seen at the metal/oxide interface correlates to the thin tetragonal-rich zirconia seen with Raman mapping. Therefore, in addition to the barriers produced by the coolant/oxide and oxide/metal interfaces, the establishment of a p-n junction between the tetragonal and monoclinic zirconia provides another required step in the oxidation mechanism of the metal substrate. This supports the theory that the tetragonal-rich layer at the metal/oxide interface is a protective barrier

to further oxidation.

SKPFM is a useful characterization technique to support the understanding of cladding oxidation mechanisms. This high-resolution, non-destructive technique can be used in the future for hydride detection and growth, oxide stoichiometry and phase distribution, secondary phases' role in cladding oxidation mechanisms, and irradiation effect of the cladding's electronic properties. When combined with complementary characterization techniques, the methods reported establish novel experimental advancements that can provide new insight into cladding degradation processes.

#### CRedit authorship contribution statement

**Corey M. Efaw:** Conceptualization, Methodology, Software, Validation, Formal analysis, Investigation, Data curation, Writing - original draft, Writing - review & editing, Visualization. **Jordan L. Vandegrift:** Methodology, Formal analysis, Investigation, Data curation, Writing - original draft. **Michael Reynolds:** Formal analysis, Investigation. **Brian J. Jaques:** Resources, Supervision, Project administration, Funding acquisition. **Hongqiang Hu:** Resources, Project administration, Funding acquisition. **Hui Xiong:** Resources, Supervision, Project administration, Funding acquisition. **Michael F. Hurley:** Conceptualization, Resources, Writing - original draft, Visualization, Supervision, Project administration, Funding acquisition.

#### Declaration of Competing Interest

The authors declare that they have no known competing financial interests or personal relationships that could have appeared to influence the work reported in this paper.

#### Acknowledgments

This work was supported in part through the Department of Energy (DOE) In-Pile Instrumentation program under DOE Idaho Operations

Office Contract DE-AC07-05ID14517. The glovebox AFM used for this work was funded through the National Science Foundation Grant No. 1727026 and accessed through the Boise State Surface Science Laboratory. The Hitachi SEM used for this work was supported by the Department of Energy [National Nuclear Security Administration] under Award Number DE-NE0000338. Paul H. Davis of Boise State University is thanked for his support with the Horiba Raman and Bruker AFM systems. The authors also acknowledge the departmental support from Boise State's Micron School of Materials Science and Engineering. The views and opinions of authors expressed herein do not necessarily state or reflect those of the U.S. Government or any agency thereof. The raw/processed data required to reproduce these findings can be shared upon request to corresponding author at coreyefaw@u.boisestate.edu.

## Appendix A. Supplementary data

Supplementary material related to this article can be found, in the online version, at doi:<https://doi.org/10.1016/j.corsci.2020.108491>.

## References

- [1] B. Cox, Pellet clad interaction (Pci) failures of zirconium alloy fuel cladding - a review, *J. Nucl. Mater.* 172 (3) (1990) 249–292, [https://doi.org/10.1016/0022-3115\(90\)90282-R](https://doi.org/10.1016/0022-3115(90)90282-R).
- [2] C.G. Yan, R.S. Wang, Y.L. Wang, X.T. Wang, G.H. Bai, Effects of ion irradiation on microstructure and properties of zirconium Alloys-a review, *Nucl. Eng. Technol.* 47 (3) (2015) 323–331, <https://doi.org/10.1016/j.net.2014.12.015>.
- [3] A.T. Motta, A. Couet, R.J. Comstock, Corrosion of zirconium alloys used for nuclear fuel cladding, *Annu. Rev. Mater. Res.* 45 (2015) 311–343, <https://doi.org/10.1146/annurev-matsci-070214-020951>.
- [4] B. Cox, Some thoughts on the mechanisms of in-reactor corrosion of zirconium alloys, *J. Nucl. Mater.* 336 (2–3) (2005) 331–368, <https://doi.org/10.1016/j.jnucmat.2004.09.029>.
- [5] H.K. Jensen, R. Szoke, N.O. Solum, A. Palencsar, PIE Results and Mechanistic Interpretation on On-Line EIS Data From the Cladding Corrosion Test IFA-731, HWR-1156, OECD Halden Reactor Project, (2017).
- [6] A. Couet, A.T. Motta, A. Ambard, D. Livigni, In-situ electrochemical impedance spectroscopy measurements of zirconium alloy oxide conductivity: relationship to hydrogen pickup, *Corros. Sci.* 119 (2017) 1–13, <https://doi.org/10.1016/j.corsci.2016.12.008>.
- [7] V. Renciuikova, J. Macak, P. Sajdl, R. Novotny, A. Krausova, Corrosion of zirconium alloys demonstrated by using impedance spectroscopy, *J. Nucl. Mater.* 510 (2018) 312–321, <https://doi.org/10.1016/j.jnucmat.2018.08.005>.
- [8] L. Kurpaska, J. Favregeon, L. Lahoche, M. El-Marssi, J.L.G. Poussard, G. Moulin, J.M. Roelandt, Raman spectroscopy analysis of air grown oxide scale developed on pure zirconium substrate, *J. Nucl. Mater.* 466 (2015) 460–467, <https://doi.org/10.1016/j.jnucmat.2015.06.005>.
- [9] L. Kurpaska, J. Favregeon, J.L. Grosseau-Poussard, L. Lahoche, G. Moulin, In-situ stress analysis of the Zr/ZrO<sub>2</sub> system as studied by Raman spectroscopy and deflection test in monofacial oxidation techniques, *Appl. Surf. Sci.* 385 (2016) 106–112, <https://doi.org/10.1016/j.apsusc.2016.05.074>.
- [10] L. Kurpaska, M. Lesniak, R. Jadach, M. Sitarz, J.J. Jasinski, J.L. Grosseau-Poussard, Shift in low-frequency vibrational spectra measured in-situ at 600 degrees C by Raman spectroscopy of zirconia developed on pure zirconium and Zr-1%Nb alloy, *J. Mol. Struct.* 1126 (2016) 186–191, <https://doi.org/10.1016/j.molstruc.2016.03.001>.
- [11] I. Idarraga, M. Mermoux, C. Duriez, A. Crisci, J.P. Mardon, Raman investigation of pre- and post-breakaway oxide scales formed on Zircaloy-4 and M5 (R) in air at high temperature, *J. Nucl. Mater.* 421 (1–3) (2012) 160–171, <https://doi.org/10.1016/j.jnucmat.2011.11.071>.
- [12] I. Idarraga, M. Mermoux, C. Duriez, A. Crisci, J.P. Mardon, Potentialities of raman imaging for the analysis of oxide scales formed on Zircaloy-4 and M5 (R) in air at high temperature, *Oxid. Met.* 79 (3–4) (2013) 289–302, <https://doi.org/10.1007/s11085-012-9331-5>.
- [13] K.B. Chong, M.E. Fitzpatrick, Evolution of stress fields and phase content in corroded zirconium cladding materials, *Surf. Coat. Tech.* 324 (2017) 140–145, <https://doi.org/10.1016/j.surfcoat.2017.05.072>.
- [14] P. Barberis, T. Merlemejean, P. Quintard, On Raman spectroscopy of zirconium oxide films, *J. Nucl. Mater.* 246 (2–3) (1997) 232–243, [https://doi.org/10.1016/S0022-3115\(97\)00038-X](https://doi.org/10.1016/S0022-3115(97)00038-X).
- [15] J. Godlewski, P. Bouvier, G. Lucazeau, L. Fayette, Stress distribution measured by Raman spectroscopy in zirconia films formed by oxidation of Zr-based alloys, *Zirconium in the Nuclear Industry: Twelfth International Symposium*, West Conshohocken, PA, 1354, 2000, pp. 877–900.
- [16] V.G. Bagotsky, *Fundamentals of Electrochemistry*, second ed., (2006) Hoboken, New Jersey.
- [17] F.N. Afshar, J.H.W. De Wit, H. Terry, J.M.C. Mol, Scanning Kelvin probe force microscopy as a means of predicting the electrochemical characteristics of the surface of a modified AA4xxx/AA3xxx (Al alloys) brazing sheet, *Electrochim. Acta* 88 (2013) 330–339, <https://doi.org/10.1016/j.electacta.2012.10.051>.
- [18] J.H.W. De Wit, Local potential measurements with the SKPFM on aluminium alloys, *Electrochim. Acta* 49 (17–18) (2004) 2841–2850, <https://doi.org/10.1016/j.electacta.2004.01.045>.
- [19] N. Sathirachinda, R. Pettersson, J.S. Pan, Depletion effects at phase boundaries in 2205 duplex stainless steel characterized with SKPFM and TEM/EDS, *Corros. Sci.* 51 (8) (2009) 1850–1860, <https://doi.org/10.1016/j.corsci.2009.05.012>.
- [20] N. Sathirachinda, R. Pettersson, S. Wessman, U. Kivisakk, J.S. Pan, Scanning Kelvin probe force microscopy study of chromium nitrides in 2507 super duplex stainless steel-implications and limitations, *Electrochim. Acta* 56 (4) (2011) 1792–1798, <https://doi.org/10.1016/j.electacta.2010.08.038>.
- [21] C.F. Mallinson, A. Harvey, J.F. Watts, Characterization of carbide particles in S-65 beryllium by scanning kelvin probe force microscopy, *J. Electrochem. Soc.* 164 (7) (2017) C342–C348, <https://doi.org/10.1149/2.0271707jes>.
- [22] C.F. Mallinson, J.F. Watts, Communication-the effect of hydrocarbon contamination on the Volta Potential of second phase particles in beryllium, *J. Electrochem. Soc.* 163 (8) (2016) C420–C422, <https://doi.org/10.1149/2.0471608jes>.
- [23] C. Senoz, S. Evers, M. Stratmann, M. Rohwerder, Scanning Kelvin Probe as a highly sensitive tool for detecting hydrogen permeation with high local resolution, *Electrochem. Commun.* 13 (12) (2011) 1542–1545, <https://doi.org/10.1016/j.elecom.2011.10.014>.
- [24] S. Evers, C. Senoz, M. Rohwerder, Hydrogen detection in metals: a review and introduction of a Kelvin probe approach, *Sci. Technol. Adv. Mater.* 14 (1) (2013), <https://doi.org/10.1088/1468-6996/14/1/014201>.
- [25] M.C. Lafouresse, M.L. De Bonfils-Lahovary, C. Charvillat, L. Oger, L. Laffont, C. Blanc, A Kelvin probe force microscopy study of hydrogen insertion and desorption into 2024 aluminum alloy, *J. Alloys. Compd.* 722 (2017) 760–766, <https://doi.org/10.1016/j.jallcom.2017.06.143>.
- [26] L. Oger, M.C. Lafouresse, G. Odemer, L. Peguet, C. Blanc, Hydrogen diffusion and trapping in a low copper 7xxx aluminium alloy investigated by scanning Kelvin Probe Force Microscopy, *Mater. Sci. Eng. A-Struct.* 706 (2017) 126–135, <https://doi.org/10.1016/j.msea.2017.08.119>.
- [27] Z.L. Hua, S.Y. Zhu, J. Shang, G.X. Cheng, Y.C. Yao, J.Y. Zheng, Scanning Kelvin probe force microscopy study on hydrogen distribution in austenitic stainless steel after martensitic transformation, *Mater. Lett.* 245 (2019) 41–44, <https://doi.org/10.1016/j.matlet.2019.02.089>.
- [28] S. Sadewasser, T. Glatzel, M. Rusu, A. Jager-Waldau, M.C. Lux-Steiner, High-resolution work function imaging of single grains of semiconductor surfaces, *Appl. Phys. Lett.* 80 (16) (2002) 2979–2981, <https://doi.org/10.1063/1.1471375>.
- [29] A. Kikukawa, S. Hosaka, R. Imura, Silicon pn junction imaging and characterizations using sensitivity enhanced kelvin probe force microscopy, *Appl. Phys. Lett.* 66 (25) (1995) 3510–3512, <https://doi.org/10.1063/1.113780>.
- [30] M.F. Hurley, C.M. Efav, P.H. Davis, J.R. Croteau, E. Graugnard, N. Biribilis, Volta potentials measured by scanning kelvin probe force microscopy as relevant to corrosion of magnesium alloys, *Corrosion* 71 (2) (2015) 160–170, <https://doi.org/10.5006/1432>.
- [31] N.N. Novik, V.G. Konakov, I.Y. Archakov, *Zirconia and Ceria Based ceramics and nanoceramics - a review on electrochemical and mechanical properties*, *Rev. Adv. Mater. Sci.* 40 (2) (2015) 188–207.
- [32] E. Polatidis, P. Frankel, J. Wei, M. Klaus, R.J. Comstock, A. Ambard, S. Lyon, R.A. Cottis, M. Preuss, Residual stresses and tetragonal phase fraction characterisation of corrosion tested Zircaloy-4 using energy dispersive synchrotron X-ray diffraction, *J. Nucl. Mater.* 432 (1–3) (2013) 102–112, <https://doi.org/10.1016/j.jnucmat.2012.07.025>.
- [33] I. Kratochvílová, R. Škoda, J. Škarohlíd, P. Ashcheulov, A. Jäger, J. Racek, A. Taylor, L. Shao, Nanosized polycrystalline diamond cladding for surface protection of zirconium nuclear fuel tubes, *J. Mater. Process. Technol.* 214 (11) (2014) 2600–2605, <https://doi.org/10.1016/j.jmatprotec.2014.05.009>.
- [34] F.J. Williams, C.M. Aldao, On the origin of metal film work function changes under electrochemical modification, *Surf. Sci.* 425 (1) (1999) L387–L392, [https://doi.org/10.1016/S0039-6028\(99\)00253-8](https://doi.org/10.1016/S0039-6028(99)00253-8).
- [35] J.L. Vandegriff, P.M. Price, I.J. Van Rooyen, S. Morrell, D.P. Butt, B.J. Jaques, Oxidation behavior of zirconium, Zircaloy-3, Zircaloy-4, Zr-1Nb, and Zr-2.65Nb in air and oxygen, *Nucl. Mater. Energy* (2019), <https://doi.org/10.1016/j.nme.2019.100692>.
- [36] C.M. Efav, T. Da Silva, P.H. Davis, L. Li, E. Graugnard, M.F. Hurley, Toward improving ambient volta potential measurements with SKPFM for corrosion studies, *J. Electrochem. Soc.* 166 (11) (2019) C3018–C3027, <https://doi.org/10.1149/2.0041911jes>.
- [37] O-Zr Phase Diagram, ASM Int., Diagram No. 101191 (2009).
- [38] C. Cardell, I. Guerra, An overview of emerging hyphenated SEM-EDX and Raman spectroscopy systems: applications in life, environmental and materials sciences, *Trac-Trends Anal. Chem.* 77 (2016) 156–166, <https://doi.org/10.1016/j.trac.2015.12.001>.
- [39] C. Duriez, T. Dupont, B. Schmet, F. Enoch, Zircaloy-4 and M5 (R) high temperature oxidation and nitriding in air, *J. Nucl. Mater.* 380 (1–3) (2008) 30–45, <https://doi.org/10.1016/j.jnucmat.2008.07.002>.
- [40] C. Duriez, D. Drouan, G. Pouzadoux, Reaction in air and in nitrogen of pre-oxidised Zircaloy-4 and M5 (TM) claddings, *J. Nucl. Mater.* 441 (1–3) (2013) 84–95, <https://doi.org/10.1016/j.jnucmat.2013.04.095>.
- [41] M. Steinbrück, M. Botcher, Air oxidation of Zircaloy-4, M5 (R) and ZIRLO (TM) cladding alloys at high temperatures, *J. Nucl. Mater.* 414 (2) (2011) 276–285, <https://doi.org/10.1016/j.jnucmat.2011.04.012>.
- [42] D.L.A. Defaria, S.V. Silva, M.T. Deoliveira, Raman microspectroscopy of some iron oxides and oxyhydroxides, *J. Raman Spectrosc.* 28 (11) (1997) 873–878, [https://doi.org/10.1002/\(Sici\)1097-4555\(199711\)28:11<873::Aid-Jrs177>3.3.Co;2-2](https://doi.org/10.1002/(Sici)1097-4555(199711)28:11<873::Aid-Jrs177>3.3.Co;2-2).
- [43] M.G.S. Ferreira, M. Da Cunha Belo, N.E. Hakiki, G. Goodlet, M.F. Montemor, A.M.P. Simões, Semiconducting properties of oxide and passive films formed on AISI 304 stainless steel and Alloy 600, *J. Braz. Chem. Soc.* 13 (4) (2002), <https://doi.org/10.1590/s0103-50532002000400005>.